

<https://doi.org/10.1038/s41529-025-00629-z>

Intragranular strain and mosaicity in Cu thin films during fast thermomechanical fatigue

Check for updates

T. Ziegelwanger¹✉, M. Reisinger², M. Petersmann², S. Van Petegem³, R. Rodriguez-Lamas⁴, J. Todt¹, M. Meindlhuber¹, J. Keckes¹ & C. Yildirim⁴

Modern high-power semiconductor devices in automotive applications are subjected to overload pulses with heating rates up to $10^6 \text{ K} \cdot \text{s}^{-1}$, causing temperature spikes of up to $300 \text{ }^\circ\text{C}$. Cu thin films in these devices function not only as electrical conductors but also as primary heat sinks, facilitating rapid thermal dissipation. This study investigated thermomechanical fatigue in Cu thin films under application-relevant conditions within a $100\text{--}400 \text{ }^\circ\text{C}$ temperature range. High-frequency (20 kHz) X-ray diffraction measurements revealed compressive stresses of up to -293 MPa , surpassing the yield strength of bulk Cu. Dark-field X-ray microscopy tracked selected grains in situ over 1000 applied cycles, with either $200 \text{ }\mu\text{s}$ or 20 ms pulse lengths. The observed grains exhibited a pronounced tendency to develop low-angle grain boundaries, which interacted with high-angle boundaries and led to constrictions in the grain shape. Structural inhomogeneities exhibited localized alternating tensile and compressive 2nd-order strains, connecting them to strain localization and deterioration of electric properties.

Since the advent of microelectronics, the layering of highly dissimilar materials, such as semiconductors, metals, ceramics, and plastics, has been known to induce residual stress¹. In case of malfunction, microelectronic devices face ultra-fast heating with rates up to $10^6 \text{ K} \cdot \text{s}^{-1}$, caused by power dissipation. Subsequently, the heterostructures mismatch in coefficients of thermal expansion (CTE) causes high thermal stress, which has been shown to potentially limit the device lifetime^{2,3}. Understanding thermal stress and its effect on the degradation of the materials' mechanical and electric properties is not just a theoretical pursuit but a crucial aspect of ensuring the reliability and longevity of microelectronic devices. New challenges arise from the increasingly complicated architecture of 3D integrated circuits or increased demands in performance and reliability⁴.

Thermal stress in microelectronic multilayers has been investigated mainly using methods such as X-ray diffraction (XRD)^{5,6}, wafer curvature^{7–10} or cantilever bending^{11,12}, combined with imaging methods such as scanning electron microscopy (SEM) or transmission electron microscopy (TEM). While the approaches have significantly advanced our understanding of thermal stresses at low heating rates of $10^{-1}\text{--}10^3 \text{ K} \cdot \text{s}^{-1}$, where creep dominates deformation, further research is needed at higher heating rates of up to $10^6 \text{ K} \cdot \text{s}^{-1}$ ⁴, to capture plastic deformation at application-relevant conditions. Moser et al. used

dedicated test structures named *polyheaters*¹³ to cycle Cu interconnect lines at heating rates of up to $10^6 \text{ K} \cdot \text{s}^{-1}$, showing that short pulses cause brittle fracture while longer pulses lead to ductile deformation¹⁴. The fractured samples showed significantly higher electrical resistance at comparable stages of fatigue, compromising the device's functionality. The influence of ultra-fast heating rates was also investigated in our recent work, where an almost five-fold increase in compressive stress (from -59 to -276 MPa) was observed for heating rates of 10^{-1} and $10^6 \text{ K} \cdot \text{s}^{-1}$, respectively¹⁵. These findings indicate that ultra-fast heating suppresses creep by inducing high strain-rate deformation, thereby modifying dislocation dynamics and interaction mechanisms.

Typically, work hardening of fcc metals with medium to high stacking fault energy (SFE) results in a hierarchical subdivision of the microstructure as dislocations align in low angle grain boundaries (LAGBs) to form wall and cell structures^{16,17}. Such a behavior is called dynamic recovery and is observed in Cu thin films with grains larger than $1 \text{ }\mu\text{m}$, as otherwise dislocations form tangles or pile up at high-angle grain boundaries (HAGBs)⁸. These cell structures occur commonly in monotonic loading but also fatigue. A phenomenon worth noting in Cu thin films' fatigue is the formation of persistent slip bands (PSBs)^{6,18}. Such PSBs may form in Cu grains larger than $1 \text{ }\mu\text{m}$ under symmetrical loads and small strains¹⁹. Therefore, PSBs can

¹Department Materials Sciences, Montanuniversität Leoben, Leoben, Austria. ²KAI – Kompetenzzentrum Automobil- und Industrieelektronik GmbH, Villach, Austria. ³Structure and Mechanics of Advanced Materials, Paul Scherrer Institute, Villigen, Switzerland. ⁴European Synchrotron Radiation Facility, Grenoble, France. ✉e-mail: tobias.ziegelwanger@unileoben.ac.at

be ruled out in the case of thermal overload pulses, as the loads are highly unsymmetrical and exceed the yield strength of Cu.

As Cu is yielding and LAGBs are formed, these sites of high dislocation density, i.e., high deformation, also facilitate the rearrangement of dislocations via dislocation climb to form vacancies. For example, severe plastically deformed Cu has been shown to have a three orders of magnitude higher vacancy concentration in LAGBs than in the surrounding material²⁰. The link between LAGBs with high vacancy concentrations and voiding in fcc metals has been established by Noell et al. for different high-purity fcc metals under monotonic loading conditions^{21–23}. Previously, voids were thought to occur through the decohesion of second-phase particles mainly²⁴. Their results showed that while nanoscale voids formed throughout high-purity Cu, only those near LAGBs grew to the micrometer scale. The absence of a clear correlation between LAGB misorientation and void size suggests that strain relief does not drive void growth. It is rather vacancy condensation in areas of high dislocation density, which is prominent in fcc metals due to dislocation climb²³.

To recapitulate, the literature indicates that intragranular structural defects and local strain gradients are linked to morphological changes, including void formation and cracking at HAGBs in fatigued Cu. Therefore, researchers have investigated the impact of thermal stress on the microstructure of Cu using electron microscopy. However, an experimental setup based on SEM and electron backscatter diffraction (EBSD) can only give limited spatial and angular resolution^{10,25}. In other instances, TEM was used to characterize samples prepared at different stages of fatigue to investigate the defect structure^{3,26}. However, research would benefit from the ability to choose a single grain in the Cu thin film and track the in situ evolution of LAGBs and strains to gain deeper insight into underlying degradation mechanisms.

Dark-field X-ray microscopy (DFXM) is a high-resolution, non-destructive technique for probing individual grains in bulk materials with high spatial and angular sensitivity^{27–29}. Previously, studies on defect structures in single-crystal Al have used DFXM to reveal how dislocation patterning and cell formation evolve through stochastic multiplicative processes, starting from randomly appearing dislocation entanglements that grow and subdivide^{30,31}. Building on our previous ex situ study of Cu thermomechanical fatigue³², where *polyheater* experiments revealed defect accumulation and HAGB cracking but lacked insight into intermediate stages, we now use in situ DFXM to track intragranular microstructural changes during early-stage fatigue. In this work, we directly observe dislocation interactions and defect evolution under cycling conditions. Additionally, 20 kHz X-ray diffraction characterizes thermal stress evolution in real-time, while EBSD provides a complementary view of the overall microstructure.

Results

To investigate thermomechanical fatigue in Cu, two types of in-situ synchrotron experiments were conducted using the *polyheater* device presented in Section "Thermomechanical testing through polyheaters". The core of this study focuses on DFXM characterization conducted at the former ID06 HXM (now ID03) beamline of the European Synchrotron Radiation Facility (ESRF) during single and multiple thermal cycling. Complementary results from the in situ high-frequency (20 kHz) XRD characterization of Cu metallization at the ADDAMS beamline of the Swiss Light Source are presented.

Orientation scans were used to determine changes in the grains' intragranular orientation (mosaicity) by tilting around the φ and χ axes while keeping 2θ constant (Fig. 1). For each pixel, the intensities at different φ -angles were used to calculate the center of mass (CoM_φ) and full width at half maxima (FWHM_φ) of the measured reflections. *Axial strain scans* were used to quantify 2nd-order strains by rotating φ and 2θ , keeping χ constant. The $\text{CoM}_{2\theta}$ was used to calculate the Cu {111} lattice plane spacing d^{Cu111} . A change in the grains average d^{Cu111} equals the build-up or relaxation of 1st-order strains, while a change of the intragranular d^{Cu111} distribution equals the 2nd-order strains. Since the sample was mounted upright (Fig. 1) and φ

was tilted in close proximity to 0° , the 1st-order strains corresponded to the in-plane direction of the sample. A benefit of the two tilt angles is the additional set of φ -rocking curves at each 2θ position. From these rocking curves, CoM_φ and FWHM_φ can also be calculated and compared to *orientation scans*, which may be beneficial due to the lower sample shift of the *axial strain scans*. A detailed description of the DFXM experiment is outlined in Section "Dark-field X-ray Microscopy".

The first single-cycle experiment investigated a 20 μm Cu thin film using DFXM (Fig. 1) at different temperature steps. This experiment aimed to observe the initial microstructure of Cu and how the elevated temperature affects existing dislocation structures and local strain. Since the individual scans took approximately one hour at every applied temperature, the single-cycle experiment corresponds to a slow heating profile present in an annealing process during manufacturing or a wafer curvature experiment.

The second in situ DFXM synchrotron experiment examined the early stages of fatigue by repeatedly cycling two 5 μm thick Cu films between 100–400 $^\circ\text{C}$ with rapid heating pulses of 200 μs and 20 ms length. Such temperature profiles mimic the overload pulses encountered during a malfunction in power electronic applications. This experiment investigated early-stage thermomechanical fatigue as intragranular dislocation structures form and interact with the HAGBs and 2nd-order strain fields. The different pulse lengths were selected to investigate the influence of increased average temperature on microstructure and strain fields.

Single-cycle experiment

From the near-field detector, a single grain from the 20 μm Cu thin film was selected for investigation using DFXM. The thin film was heated to 400 $^\circ\text{C}$ in multiple 100 $^\circ\text{C}$ steps and cooled down to room temperature. DFXM was conducted at each heating step to examine the initial internal microstructure of the selected Cu grain and its response to a slow heating cycle.

The local CoM_φ in Fig. 2a were obtained through *orientation scans* and represent the inclination of the Cu {111} lattice plane normal to the experimental φ -axis (Fig. 1). Any grain that deviates from a perfect single crystal will exhibit a spread in CoM_φ due to natural misorientation from structural defects and mosaicity. The local mappings of the CoM_φ are presented in Fig. 2a, clockwise from heating to cooling. Differently oriented

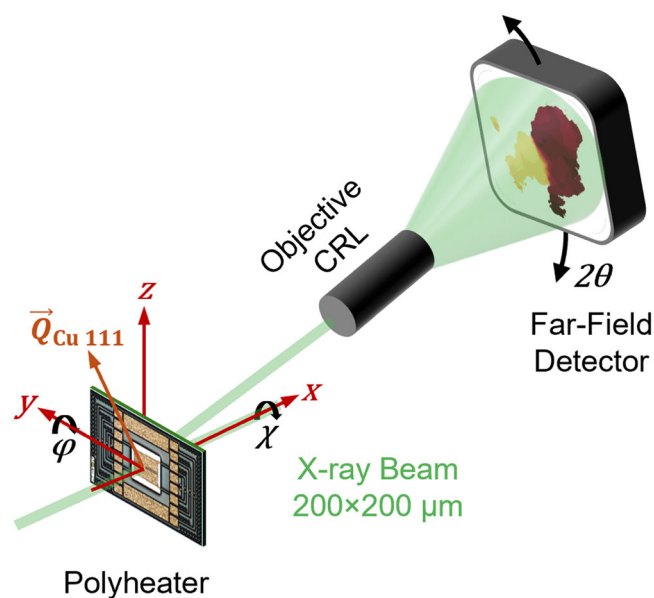
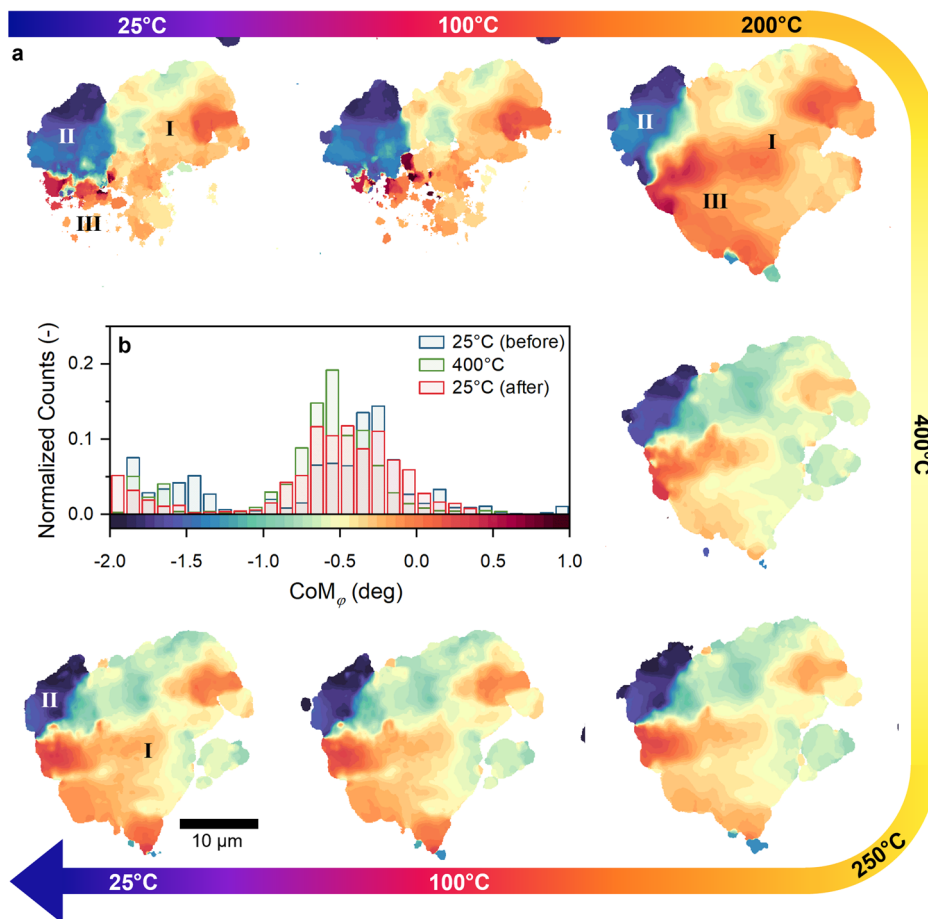


Fig. 1 | A schematic of the DFXM experiments. The schematic outlines the DFXM experiments performed at the former ID06 HXM beamline at the ESRF. The sample was scanned in transmission mode. A diffraction spot chosen from the Cu 111 DS-ring was magnified by a CRL objective on the downstream far-field detector. 2D orientation scans were conducted by tilting along the φ - χ axes, and 2D axial strain scans were conducted by mapping the φ - 2θ axes.

Fig. 2 | Evolution of orientation during a single heating cycle. For the single heating cycle, the CoM_φ were obtained through *orientation scans* at different temperatures between 25 and 400°. The local mappings are shown clockwise from heating to cooling (a). Histograms of the CoM_φ distribution at 25° and 400° are shown in the center (b). The scale bar of the local mappings is shown on the x -axis of the histogram. The fragmented grain showed homogenization at 200 °C and overall rotated towards lower φ angles.



parts of the grain, such as dislocation cells have been identified and labeled sections. The CoM_φ of the initial grain was mainly oriented at an φ -angle of -0.32° , shown in orange and green colors, and was marked as section I. The dark blue cell in the grain's upper left was marked as section II and was oriented at an average φ angle of -1.48° , with an additional peak at -1.85° (section II). The lower part of the grain in Fig. 2a, labeled section III, appeared fragmented and dark red, indicating an φ -orientation close to the upper end of the scanning range at 1° . The overall distribution of CoM_φ for this mapping is shown in the histogram in Fig. 2b, where the different sections can be identified. Section III remained fragmented up to a temperature of 200 °C, after which it homogenized and adopted the orientation of section I at -0.22° . The now equiaxed grain showed a total diameter of approximately 30 μm. Afterward, the shape of the grain remained unchanged and rotated towards a lower φ -angle of -0.43° . Section II continuously shrank in size and rotated towards a lower CoM_φ at -2° as parts of the cell moved out of the scanning range of the φ -axis.

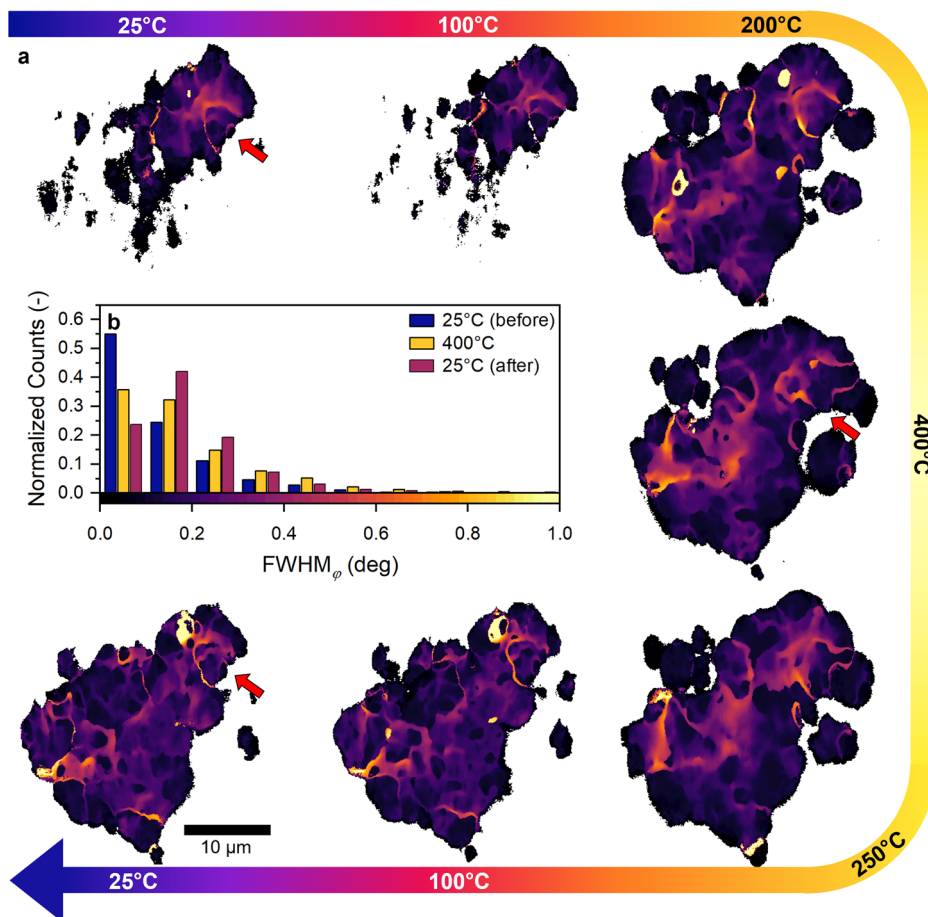
Figures 3–5 present mappings of the same grain using axial strain scans, which is why the form differs slightly from Fig. 2. The peak broadening of Cu 111 (FWHM_φ) is shown in Fig. 3 correlating to the number of defects or 2nd-order strains. For comparison, the FWHM_φ obtained through orientation scans is shown in Supplementary Fig. 1. The initial grain exhibited pronounced defect structures, as indicated by streaks of increased FWHM_φ in Fig. 3a. Due to their shape, they were mostly identified as LAGBs separating cells of different orientations within the grain. In the pristine grain at 25 °C, the red arrow shows an example of a preexisting LAGB. As the temperature increased, the thermally activated dislocation movements become more probable, increasing mobility³³. At 400 °C, the LAGB marked by the red arrow has loosened and partially merged with the HAGB to its right. The question of why the outer boundaries were identified as HAGBs and not LAGBs of higher misorientation will be addressed in the

discussion. As the Cu thin film cooled to room temperature, the LAGBs reformed and increased in FWHM_φ , as again exemplified by the LAGB marked by the red arrow. The overall development of the FWHM_φ is shown in the histogram (Fig. 3b) and displays a gradual increase throughout the single heating cycle.

In Fig. 4a, local mappings of $d^{\text{Cu}111}$ are shown. The sections I–III, identified in the orientation scan (Fig. 2a), were marked in the first mapping at 25°C. The average $d^{\text{Cu}111}$ increased throughout the heating of the Cu thin film as the color scheme changed from violet to orange. As the sample cooled, the average $d^{\text{Cu}111}$ remained elevated, indicating the formation of 1st-order tensile strain. This trend is highlighted in Fig. 4b, where the average $d^{\text{Cu}111}$ was plotted at different temperature steps. At room temperature, the lattice plane spacing amounted to $2.084 \pm 3 \times 10^{-4}$ Å, which is slightly lower than expected for the Cu thermodynamic equilibrium of 2.087 Å. Based on the initial $d^{\text{Cu}111}$, the theoretical lattice plane spacing at elevated temperatures was calculated assuming linear thermal expansion. This assumption was valid for the heating process as $d^{\text{Cu}111}$ increased to $2.096 \pm 2 \times 10^{-4}$ Å, for the maximum temperature of 400 °C. However, as visible in the local mappings, the $d^{\text{Cu}111}$ remained elevated after cooling below 250 °C. At 25 °C, the average $d^{\text{Cu}111}$ was $2.090 \pm 3 \times 10^{-4}$ Å, which is considerably higher than the initial value of $2.084 \pm 3 \times 10^{-4}$ Å and the thermodynamic equilibrium, indicating a 1st-order tensile strain in in-plane sample direction. The 1st-order strains amounted to $-1.4 \pm 0.1 \times 10^{-3}$ and $-1.4 \pm 0.1 \times 10^{-3}$, before and after the single cycle, respectively.

Local variations of $d^{\text{Cu}111}$ are shown through mappings of 2nd-order strain ($\epsilon^{\text{Cu}111}$) in Fig. 5a. In the pristine grain, HAGBs were sites of increased alternating tensile and compressive strains, which appeared especially at intersections with structural inhomogeneities observed in Fig. 3a. In the example marked by the red arrow in Fig. 3a, the local mapping showed a region of increased tensile strain closely tracing the LAGB. This suggests a

Fig. 3 | Evolution of defect structures during a single heating cycle. Clockwise, local mappings of the FWHM_φ obtained through axial strain scans, are displayed from heating to cooling (a). The FWHM_φ distributions at room temperature and peak temperature are shown in (b), with the color bar on the x -axis representative of the local mappings. While the average FWHM_φ increased throughout the single heating cycle, the dislocation structures lost during heating and reformed, as shown by the red arrows.



correlation between microstructural inhomogeneities and concentrations of 2nd-order strain. At 400 °C, where most of the LAGBs had loosened, the 2nd-order strains became homogeneous in the grain interior. Similar to the LAGBs, the 2nd-order strains became heterogeneous again during cooling and increased in amplitude. The histograms of the 2nd-order strains in a pristine state, at the peak temperature, and after the single-heating cycle are given in Fig. 5b. The behavior of the 1st-order strain is partially reflected as the 2nd-order strain distribution is initially skewed towards compression and skewed towards tension, after the cycle. At 400 °C, the $\epsilon^{\text{Cu}^{111}}$ showed a normal distribution around zero.

The single-cycle experiment revealed that the initial microstructure of the Cu thin film exhibited dislocation structures and relatively large intragranular mosaicity as the investigated grain was partially fragmented. The microstructure became more homogeneous as the Cu thin film underwent a temperature cycle between 25 and 400 °C, with the grain shape becoming more defined and the dislocation structures loosening up. As the LAGBs disappeared, the associated 2nd-order strains were also relieved. The dislocation structures reformed as the Cu thin film cooled, and the associated 2nd-order strains reappeared in increased amplitude.

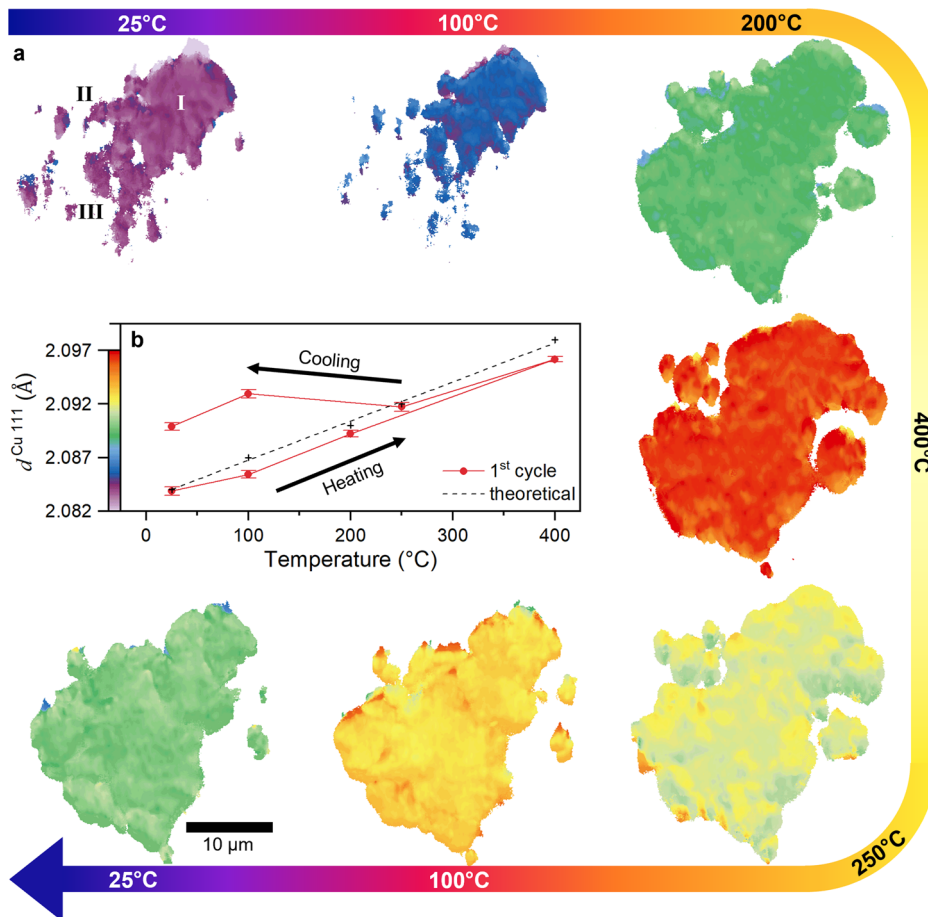
200 μs cycling experiment

Multiple thermomechanical cycles between 100–400 °C were applied to 5 μm thick Cu thin films to investigate the impact of overload pulses on the Cu thin films. However, for the interpretation of microstructural degradation, the thermal stress caused by the overload pulses is particularly interesting. Therefore, equivalent *polyheaters* were investigated using high-frequency (20 kHz) XRD at PSI. Figure 6a shows the temperature profile of those cycling pulses that had either 200 μs or 20 ms in length. The maximum temperatures measured by high-frequency XRD were 332 and 396 °C for the shorter and longer pulse lengths, respectively. The temperature profiles

measured by XRD analysis and the Al temperature sensor integrated into the polyheater are compared in Supplementary Fig. 2. The maximum compressive stresses recorded for the different pulses were -201 ± 22 and -293 ± 18 MPa for the 200 μs and 20 ms long pulses, respectively (Fig. 6b). These results indicate that the Cu thin film cycled by the shorter pulse length was exposed to less thermal stress than the Cu thin film cycled by 20 ms pulse length. The effect of these temperature cycles on the Cu microstructure is shown in Figs. 7–10.

Local mappings of the CoM_φ obtained by *orientation scans* after 1, 500, and 1000 applied cycles are shown in Fig. 7a for the short pulse duration of 200 μs. The initial Cu grain showed two distinct subgrains labeled sections I and II, with average φ orientations of 1.75° and -0.8° . A sharp LAGB separated them. After 500 applied cycles, both grains rotated towards lower φ orientations of 0.4° and -1.8° , and the orientation distribution of CoM_φ widened considerably (Fig. 7b). The initially sharp grain boundary appeared fragmented and jagged. This can also be observed in the distribution of CoM_φ visible in the histograms in Fig. 7b. To emphasize this point, the FWHM_φ of selected line profiles are shown in Fig. 7c, d for 1 and 500 applied cycles, respectively. The positions of the line profiles were indicated in the local mappings (Fig. 7a) by dotted lines in identical colors. The pristine grain showed a LAGB extending between 1–5 μm in different portions of the grain. After 500 cycles, the FWHM_φ is elevated almost across the whole grain, as well as widened up to 20 μm. Local Mappings of the FWHM_φ are shown in Supplementary Fig. 3. After 1000 applied cycles, the apparent grain shape had changed significantly, and the measured CoM_φ distribution rotated further towards lower φ orientations of -3° and -1.5° . Because of the significant shape change, no line profiles were exported from this scan. The full range of mappings for the CoM_φ and FWHM_φ of the *orientation scans* is displayed in Supplementary Fig. 2.

Fig. 4 | Evolution of lattice spacing during a single heating cycle. Clockwise, local mappings of the $d^{\text{Cu}111}$ are shown from heating to cooling (a). The average $d^{\text{Cu}111}$, obtained from axial strain scans, is displayed for different temperatures (b), with the theoretical values being calculated under the assumption of linear elastic thermal expansion. The color scale bar of the local mappings is shown in the y-axis of (b). After the single heating cycle, the lattice spacing indicates the formation of 1st-order tensile strain.



The presentation of the evolution of microstructure continues in Fig. 8 using data from *axial strain* scans, which illuminated only section II visible in Fig. 7a since the χ angle is kept constant, thus prohibiting the diffraction of section I. Mappings of the CoM_φ (Fig. 8a) showed a grain that was mainly oriented at 2° and rotated towards lower φ angles while forming cell structures. In section III, two subgrains oriented at 0.4 and -0.7° formed between 200 and 750 cycles (Fig. 8a). The LAGB becomes visible in the FWHM_φ after 200 cycles, as marked by arrows 1, and it increases from 0.4° to a bright streak of up to 1.6° after 750 cycles (Fig. 8b). A similar behavior was observed in section IV of the grain, where the initial homogeneous grain was split into three different cells. Bright streaks of increased FWHM_φ , which split the cells, were marked by arrows 2 at 200 and 750 applied cycles. In all of these cases, the formation of an LAGB led to a constriction of the grain shape, as at the LAGB-HAGB intersections. This is especially apparent in the example marked by arrow 1 after 750 cycles, where an almost circular hole appeared. These constrictions may serve as potential void nucleation sites, as reasoned in the discussion. After 1000 applied cycles, most of the grain had rotated out of the scanning range, and only small globular dislocation cells were observed (Fig. 8a). Only section V of the original grain could be traced up to 1000 cycles, rotating from -1° to -3° . The axial strain scans further gave insight into the Cu $\{111\}$ lattice plane spacing changes and intragranular strain (Fig. 8c, d). The mean $d^{\text{Cu}111}$ was $2.088 \pm 2 \times 10^{-4} \text{ \AA}$, which decreased slightly to $2.087 \pm 2 \times 10^{-4} \text{ \AA}$ between 100–750 applied cycles before decreasing further to $2.085 \pm 5 \times 10^{-4} \text{ \AA}$ after 1000 applied cycles. This indicates the formation of 1st-order compressive strains in the sample in plane direction. Local mappings of the 2nd-order strains (Fig. 8d) showed an increased amplitude near HAGB as indicated by arrows 3. As the Cu thin film was fatigued, those strains extended to the grain interior, often in the vicinity of LAGBs. In one case marked by arrows 4, it was observed how tensile strain extended into the grain's interior after 100 cycles. After

200 cycles, the $\varepsilon^{\text{Cu}111}$ formed a complex state of alternating tensile and compressive strains before that part moved out of the image at 300 cycles. After 1000 cycles, the remaining subgrains exhibited similar strain fields that span across the whole cells.

Summarized, the Cu grain cycled by the 200 μs pulses showed a tendency for hierarchical subdivision of microstructure as LAGBs formed and separated the initial grain into multiple subgrains (sections I–V). Those subgrains rotated away from the ω -orientation of the primary grain. The HAGBs exhibited increased 2nd order strains, which extended into the grain body as structural inhomogeneities formed. Additionally, the grain shape constricted at intersections of LAGBs and HAGBs, which were interpreted as void formation sites.

20 ms cycling experiment

To see potential influences of the pulse length, i.e., the longer exposure to higher temperatures, a second 5 μm Cu metallization was cycled using 20 ms pulses between 100–400 °C. *Orientation scans* revealed the local φ orientation of the selected grain in Fig. 9. The main body of the grain was oriented at an φ angle of 4.5° with little significant intragranular features and only a rather continuous gradient over the grain length. After 500 applied cycles, the grain splits into two almost equal parts labeled sections I and II, with a CoM_φ of 5° and 3.7° , respectively (Fig. 9b). After 1000 cycles, the upper part rotated out of the scanning range, and a third cell, marked as section III and oriented at 5.5° , formed. After 500 cycles, the grain started showing similar constrictions as outlined for the 200 μs pulse length, although of a greater depth. The full range of mappings for the CoM_φ and FWHM_φ of the *orientation scans* is displayed in Supplementary Fig. 3.

The CoM_φ from *axial strain* scans in Fig. 10a revealed a similar grain shape and a formation of cells. Those cells were labeled sections I–III in accordance with Fig. 9a. Section I was oriented at 5° and moved towards

Fig. 5 | Evolution of 2nd-order strains during a single heating cycle. Local variations of $d^{\text{Cu}111}$ are shown as 2nd order strain $\epsilon^{\text{Cu}111}$ for the single temperature cycle (a). The histogram in the center shows the distribution of 2nd-order strains before, at maximum, and after heating (b). The color scale of the mappings is embedded in the x-axis of (b). Regions of increased tensile strain coincide with regions of increased FWHM_φ in Fig. 3a.

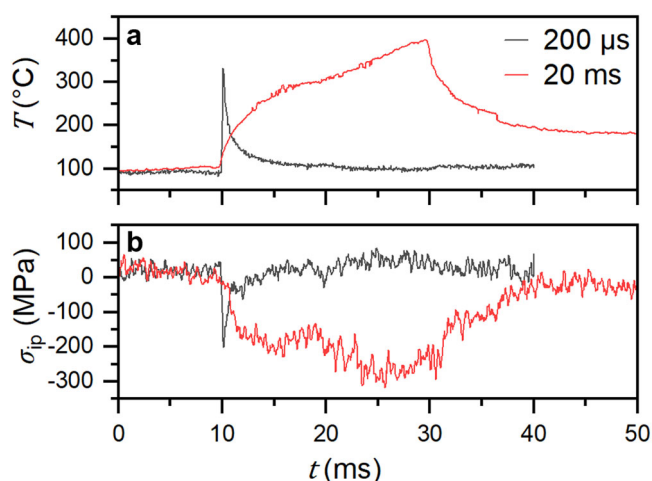
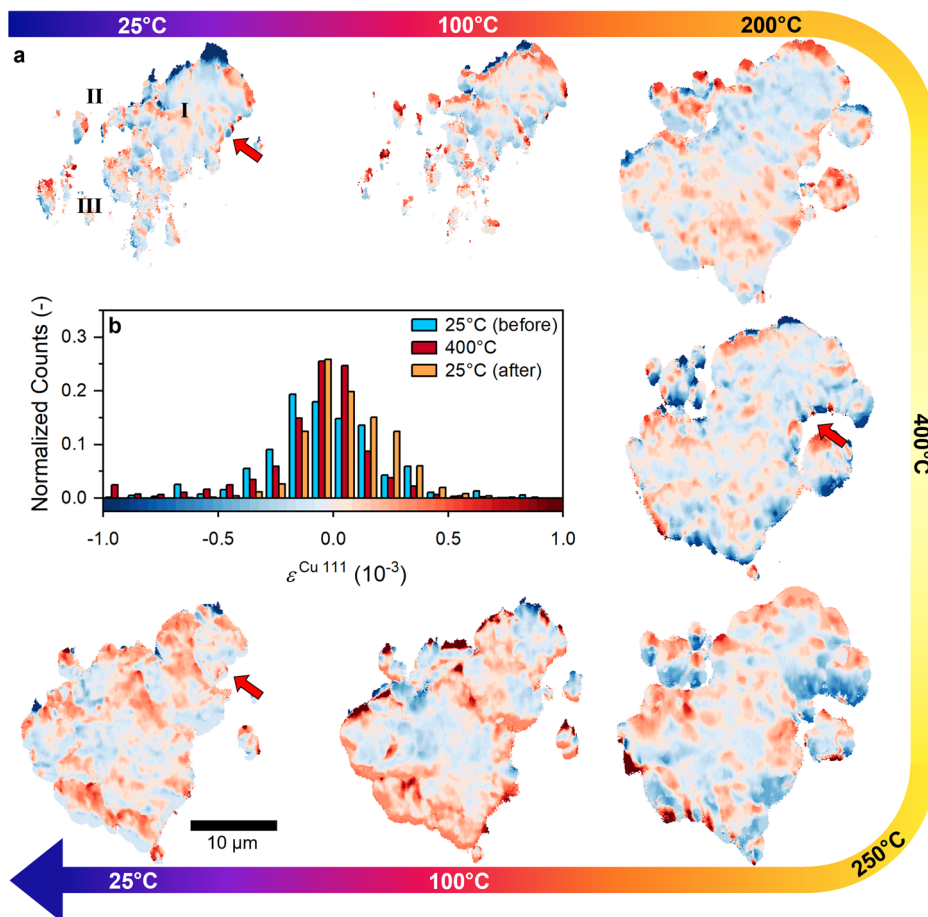


Fig. 6 | Temperature and stress profiles obtained through High Frequency XRD. Displayed are the temperature (a) and stress (b) derived from the high-frequency XRD measurements. The temperature pulses ranged from 100–400 °C and differed only in their pulse length between 200 μs and 20 ms. The maximum stresses observed were -201 ± 22 MPa and -293 ± 18 MPa for the shorter and longer pulse lengths, respectively.

higher angles as sections II and III formed after 300 and 1000 cycles, respectively. In contrast to the *orientation scans*, section II already moved out of the scanning range before 500 cycles, which indicates an additional rotation in χ . After 1000 cycles, another cell (section IV), only partly visible in the *orientation scan*, became visible. The local FWHM_φ displays the

formation of LAGBs during thermomechanical cycling (Fig. 10b) as labeled for two examples by arrows 1 and 2. The LAGB, marked by arrows 2, was formed after applied cycles separated sections I and II. Similar to the short temperature cycles, the intersections of LAGBs and HAGBs showed pronounced constrictions of the grain shape (cf. Figs. 8b, 10b). The average lattice plane spacing of the pristine grain was $2.085 \pm 2 \times 10^{-4}$ Å which increased to $2.087 \pm 2 \times 10^{-4}$ Å after 100 applied cycles and stayed constant after additional cycling (Fig. 10c). The spread of the lattice spacing increased from 2×10^{-4} to 6×10^{-4} Å with progressive thermal cycling, indicating the formation of 2nd-order strains. The local intragranular strain mappings showed alternating regions of increased tensile and compressive strain near HAGBs of the initial Cu grain (marked by arrows 3 in Fig. 10d). As thermomechanical fatigue progressed, the strain distributions within the grain interior intensified and became more complex. One pronounced feature marked by arrow 4 is a line of increased tensile strain concentration after 300 applied cycles, as opposed to spots of high compressive strain in the lower region. After 500 applied cycles, the upper area moved out of the scanning range, and only the compressively strained spots remained. After 1000 cycles, the alternating stresses close to the HAGBs were reduced. Instead, the area close to the HAGB was in compressive strain, while the interior was strained in tension.

To recapitulate, the Cu grain cycled by the 20 ms long pulses showed a similar microstructural degradation as for the 200 μs pulses. The mosaicity of the grain increased as cell structures formed and strains extended from HAGBs into the grain body. The grain shape also showed significant constriction at intersections of LAGBs and HAGBs.

Multiple pulsed – EBSD measurements

EBSD characterization was performed on three electrochemically polished *polyheaters* to compare the microstructure across multiple grains with the

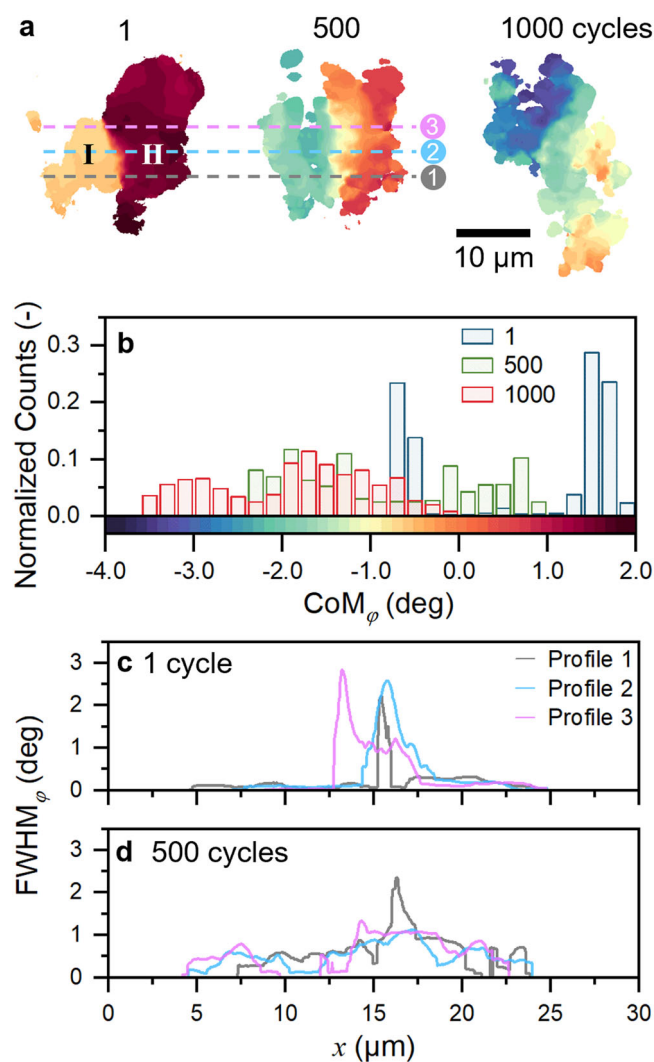


Fig. 7 | Orientation scans during early-stage fatigue using 200 μs heating pulses. Local CoM_ϕ mappings of a selected grain after cycling between 100 and 400 °C, with 200 μs pulse length, for 1 cycle, 500 cycles, and 1000 cycles are displayed (a). The histogram (b) shows the initial CoM_ϕ mean values of the individual subgrains at -0.6° and 1.7° and their development after 500 and 1000 cycles. Line profiles of the FWHM_ϕ are shown after 1 cycle (c) and 500 cycles (d). The position of the line profiles is marked by dotted lines in (a).

observations from DFXM. Of the three samples prepared, one was in a pristine state (Fig. 11a), and the other two were cycled 1000 times between 100–400 °C with either 200 μs or 20 ms pulse length. SEM images of the polished surfaces are shown in Supplementary Fig. 5, where a great number of voids can be observed in the fatigued samples. However, to draw better comparison to DFXM smaller areas have been scanned with high-resolution EBSD (HR-EBSD). From top to bottom, the band channel contrast, orientation, and (kernel-average misorientation) KAM are shown with white pixels marking spots where no valid fit of the Kikuchi pattern was possible. Examining the band contrast images, the Cu thin films exhibited grains with a size of roughly 3–5 μm . No significant grain growth or grain rotation was observed when comparing the band channel contrast and orientation in Fig. 11a–c. Differences become only apparent when comparing the KAM of the respective stages of fatigue. First, the overall KAM increased from the pristine state to the sample cycled with 200 μs long pulses and further to the sample cycled with 20 ms long pulses. However, the greater change lies in the formation of bright streaks of increased KAM, which are attributed to the formation of subgrain boundaries similar to the observations in DFXM. While the pristine sample only exhibited three such

LAGBs (Fig. 11a), the number greatly increased with thermal loading as multiple LAGBs were visible in the fatigued samples (Fig. 11b, c). The histograms of the KAM mappings are shown in Supplementary Fig. 6.

Discussion

Any semiconductor/metal interface will exhibit thermomechanical stress due to the large differences in CTE, such as $18.42 \times 10^{-6} \text{ K}^{-1}$ and $3.62 \times 10^{-6} \text{ K}^{-1}$ for Cu and Si, respectively^{34,35}. After the electrochemical deposition (ECD) of the Cu film, the polyheater was exposed to an annealing treatment at 400 °C for 30 min. This leads to a stable microstructure and induces tensile stresses between 100–200 MPa during cooling^{10,36}. Such tensile residual stress is comparable to the 110 MPa observed in this study. Heating the sample to 400 °C, led to a maximum compressive stress of -201 ± 22 and -293 ± 18 MPa for the 200 μs and 20 ms long pulses (Fig. 6). The difference may have been due to the different maximum temperatures of 332 and 396 °C for the shorter and longer pulse length, respectively. A reason for the different peak temperatures might have been the higher temperature gradient between the heating layer, the Al sensor, and Cu for the shorter pulse length compared to the longer³⁷. The maximum compressive stress of -293 ± 18 MPa was higher than the -276 MPa observed for a temperature pulse between 25–525 °C in the prior study of the authors¹⁵. Other investigations on the yield strength of Cu under compression have measured an increasing yield strength of Cu at room temperature of 330 MPa, 350 MPa, and 400 MPa for strain rates of 10^{-1} , 10^1 , and 10^3 s^{-1} , respectively^{38,39}. The reason why a lower maximum compressive stress still results in yielding can be directly related to the elevated temperature, which decreases the resistance of Cu towards deformation⁴⁰.

The impact of the thermal stress cycles on the microstructure of Cu was investigated using DFXM and EBSD. One distinct difference between the two characterization methods is already seen in the pristine metallization, where the grain size observed by EBSD was between 3–5 μm (Fig. 11a). In contrast, the grains observed by DFXM spanned several tens of micrometers (Fig. 2). Since the Cu thin films were electrochemically deposited (ECD), abnormal grain growth is a common phenomenon rooted in Cu's elastic anisotropy, the energies of different types of Cu grain boundaries, and the preferential adsorption of additives⁴¹. As the grains observed by DFXM were selected prior from the DS-ring on the near-field detector, there was a bias towards selecting the diffraction spots with the highest intensity, *i.e.*, the largest grain in the irradiated volume. Results show that despite the annealing step after the Cu deposition, plenty of dislocations and large structures such as LAGBs were still present (cf. Figs. 3a, 11a). One issue is the difficult differentiation of LAGBs and HAGBs with misorientations below or above 15° , respectively. Since the ϕ angle was only tilted in a range of $3\text{--}6^\circ$, the differentiation between a HAGB and a LAGB with a misorientation above 6° was difficult. However, the KAM measured by EBSD (Fig. 11a, Supplementary Fig. 6) showed that preexisting LAGBs have a low misorientation. Therefore, the outer boundaries of the grains are most probably HAGBs. The single-cycle experiment between 25–400 °C acted as an additional annealing step, further homogenizing the grain shape. The lattice spacing showed a pronounced formation of 1st-order tensile strain after the single-cycle, which localized at structural inhomogeneities such as LAGBs. At elevated temperatures, those LAGBs became more diffuse, as minimizing the grain's free energy through reducing stacking faults became less important^{42,43}. As the Cu thin film cooled down, the LAGBs became distinct again, and FWHM increased due to the incorporation of newly formed dislocations. The overall formation of LAGBs during applied loads is called dynamic recovery.

Dynamic recovery was also observed in the early-stage fatigue experiments of this study, where the time for dislocation movement was smaller in orders of magnitude. While it may not be expected for the single cycle sample and the fatigued samples to show similar deformation behaviors, Zhang et al. has shown that deformation mechanisms in Cu thin films above 1 μm thickness are comparable to those of bulk Cu⁸. As LAGBs formed, they led to a hierarchical subdivision of microstructure in subgrains, which rotated towards beneficial orientations. This increased the overall

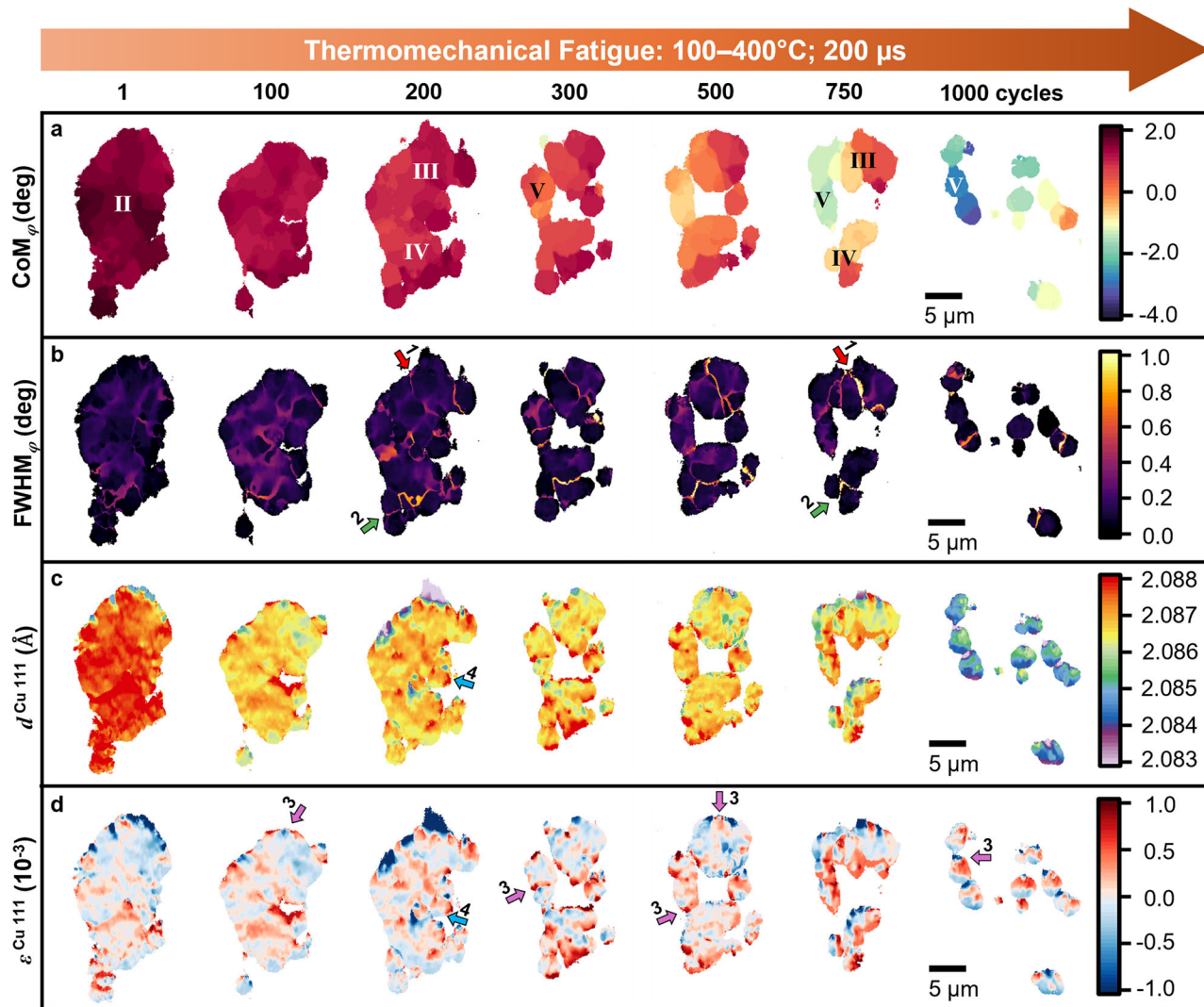


Fig. 8 | Early-stage fatigue during up to thousand 200 μ s short heating pulses. Mappings of the axial strain scans at different stages of cycling between 100 and 400 $^{\circ}$ C, with 200 μ s pulse length, are shown. The images display the CoM_{φ} (a),

FWHM_{φ} (b), $d^{\text{Cu}111}$ (c), and $\varepsilon^{\text{Cu}111}$ (d). The scale bars on the right side of the image are valid for all mappings. The labeled arrows point towards structural features of interest outlined in the main text.

mosaicity of the grain, as observed in the histograms in Figs. 7b and 9b. Although the hierarchical subdivision was also observed in EBSD scans (Fig. 11), DFXM has proved far greater sensibility for subgrain formation as it could track minute changes in orientation. Additionally, it was possible to track 2nd-order strains in the vicinity of newly formed LAGBs and HAGBs. As temperature cycles were applied, the existing tensile and compressive strains along the HAGBs extended into the grain's interior. This generally happened along LAGBs and caused a hardening of that region. In some cases, the LAGBs acted as clear separations between areas strained in tension and in compression. Those strains increased significantly for the shorter pulse lengths of 200 μ s, indicating increased plastic deformation.

The HAGB-LAGB intersections showed not only strain localization but also a constriction of the grain shape. Similar constrictions have been found in recrystallizing Al, where constrictions in the grain shape were connected to mosaic structures of ultra-low-angle grain boundaries⁴⁴. Therefore, such constrictions are either possible through a neighboring grain growing or the formation of voids. Compared to other studies on fatigued Cu thin films, voiding is a common phenomenon observed along with the formation of intrusions and extrusions^{5,23,32}. Such voids appear in high-purity fcc metals even without second-phase particles, as recent studies have shown for monotonic^{22,23} and cyclic loading^{5,6}. Those

voids appeared close to areas of high dislocation densities (i.e., LAGBs), similar to observations in this study. A possible mechanism was formulated through the annihilation of edge dislocations in dislocation walls, creating vacancies. Those vacancies diffuse towards HAGB or triple points, condensing to form pores. Signs of such behavior were evident in the grains observed in this study throughout the process of thermomechanical fatigue (Figs. 8, 10).

The length of overload pulses was a deciding factor for the potential cracking of HAGBs. Moser et al. fatigued two Cu lines with 12000 temperature cycles between 145–445 $^{\circ}$ C and pulse lengths of either 200 μ s or 5.4 ms¹⁴. Results have shown that the shorter pulse length resulted in pronounced voiding and cracking of Cu. In contrast, the longer pulse length led to the formation of intrusions and extrusions, increasing surface roughness due to creep and diffusion phenomena. This is very important for the lifetime of the final devices as cracking affects the electrical conductivity far more than surface roughness. Ex situ studies using DFXM have associated the cracking of HAGBs with the pile-up of dislocations at the near-HAGBs, causing strain localization and hardening³². In the present study, it was observed that all pristine grains exhibited alternating strains at the grain boundaries, indicating significant shear stress. Those alternating strain fields increased and extended into the grain interior and also in the vicinity of

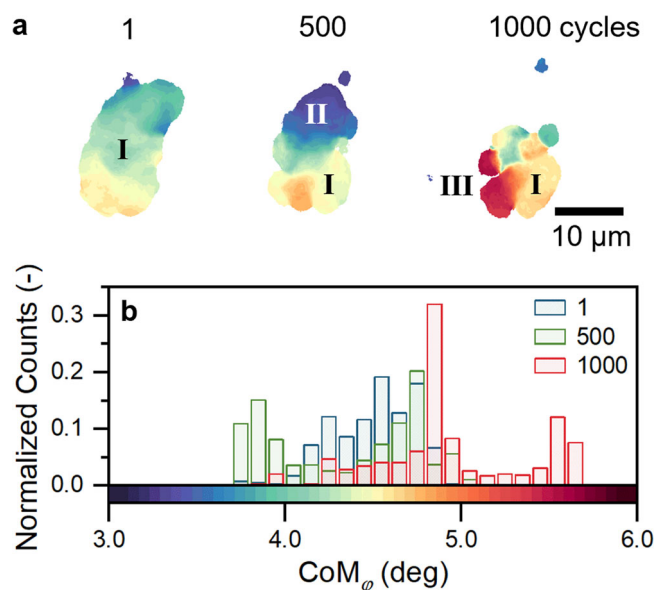


Fig. 9 | Orientation scans during early-stage fatigue using 20 ms long heating pulses. CoM ϕ mapping of the Cu thin film after cycling between 100 and 400 °C, with 20 ms pulse length for 1 cycle (a), 500 cycles (b), and 1000 cycles (c). The histogram in (d) shows the initial CoM ϕ mean value around 4.6°. Cycling shifted towards 3.7° after 500 pulses before parts of the grain started turning out of the scanned range of ϕ .

LAGBs. Comparing Fig. 8d and 10d, it became apparent that the local strain concentrations of the short pulse lengths were higher for the 200 μ s than for the 200 ms pulse length. The larger shear strain promotes an increased formation of LAGBs, acting as sources and pathways for vacancies to form pores. The combination of pores, increased shear strains, and a hardening of the near-HAGB finally leads to cracking in Cu.

Ex situ DFXM studies have previously linked HAGB cracking to dislocation pile-ups, leading to strain localization and local hardening. This study expands on these findings by showing that pristine Cu grains already exhibit alternating shear strain fields at grain boundaries. During thermomechanical cycling, these shear strains intensify and extend into the grain interior, particularly near LAGBs. Short thermal pulses further amplify localized shear strain and promote vacancy diffusion, accelerating void formation and crack initiation. The results indicate that the combined effects of void growth, increased shear strain, and HAGB hardening play a critical role in Cu failure under short-pulse thermal cycling.

This study investigated early-stage thermomechanical fatigue in Cu thin films exposed to high heating rates (10^6 K \cdot s $^{-1}$), revealing key microstructural changes for Cu interconnect reliability. DFXM revealed a significant defect structure and strain localization at HAGBs for the pristine Cu grain. The slow single-cycle experiment (25–400 °C) showed how dislocations loosen at elevated temperatures and reform during cooling. The reformed boundaries showed increased misorientation and increased local 2nd-order tensile strains. Applying cyclic loading between 100–400 °C, compressive stresses of up to -293 MPa induced significant plastic deformation, promoting the formation of LAGBs and subgrain rotation. As LAGBs formed, local 2nd-order strains increased and extended from the HAGBs to the grain interior. Shorter pulse lengths (200 μ s) intensified strain localization, suggesting increased hardening and crack susceptibility. As Cu was fatigued, the grain shape showed constrictions at HAGB-LAGB intersections, which were attributed to void formation. Therefore, Voiding was linked to vacancy diffusion from regions of high dislocation density. These findings clarify the role of LAGB evolution in fatigue-induced void formation and provide insights for enhancing Cu interconnect durability in high-power microelectronics.

Methods

Thermomechanical testing through polyheaters

This study used dedicated test chips called *polyheaters*¹³. The key functional layers are the highly resistive polycrystalline Si (Si_{poly}), the Al temperature sensor, and the Cu thin film. Those layers were stacked onto a 120 μ m thick industrial grade Si (100) wafer and electrically isolated by SiO₂. Between the last SiO₂ layer and the Cu thin films, a 350 nm thick WTi adhesion layer was deposited. The Cu thin film was synthesized at room temperature using electrochemical deposition using similar conditions as Moser et al.¹⁴. Afterwards, the *polyheater* was annealed for 30 minutes at 400 °C to achieve a stable Cu microstructure.

The *polyheater* was connected to a dedicated electrical setup for the generation of rapid electric pulses. Applying voltage to the Si_{poly} layer led to ohmic heating of the entire *polyheater* stack, which was measured by the temperature-dependent resistivity of Al. Thereby, key parameters for the different temperature cycles were calibrated, i.e., base temperature (T_{base}), peak temperature (T_{peak}), and pulse length (t_{pulse}). First, a 20 μ m thick Cu thin film was subjected to a constant voltage, to heat the *polyheater* to a T_{base} between 25–400 °C and characterized using DFXM. Second, two 5 μ m thick Cu thin films were cycled between 100–400 °C by applying short power pulses in addition to the constant voltage ($T_{\text{base}} = 100$ °C). The samples were heated to a T_{peak} of 400 °C within 200 μ s or 20 ms. Between two adjacent pulses, a waiting time of 1 s ensured the cooling of the *polyheater* back to T_{base} . All experiments were conducted in an ambient environment. The total imposed strain ϵ_{th} and strain-rate $\dot{\epsilon}_{\text{th}}$ on the Cu thin film were calculated based on the CTE (α) mismatch between Si and Cu:

$$\epsilon_{\text{th}} = (\alpha_{\text{Si}} - \alpha_{\text{Cu}}) (T_{\text{peak}} - T_{\text{base}}) \quad (1)$$

$$\dot{\epsilon}_{\text{th}} = \frac{\epsilon_{\text{th}}}{t_{\text{pulse}}} \quad (2)$$

Since the CTEs are temperature dependent, a mean value for the investigated temperature range was calculated using polynomial descriptions from literature^{34,35}. The used values were 18.42×10^{-6} K $^{-1}$ and 3.62×10^{-6} K $^{-1}$ for Cu and Si, respectively. Therefore, the total imposed strain was 0.44% at a rate of 22 s $^{-1}$ or 0.22 s $^{-1}$ for the 200 μ s and 20 ms long pulses, respectively.

Dark-field X-Ray microscopy

Thermomechanical fatigue within single Cu grains was observed using DFXM at the former ID06-HXM (now ID03) beamline at the European Synchrotron Radiations Facility in Grenoble (ESRF), France¹⁵. For this experiment, an X-ray photon energy of 17 keV was selected using a Si(100) double crystal monochromator. A compound refractive lens with 14 Be lenslets focused the beam to a 200 \times 200 μ m spot size, which was larger than the expected grain size of Cu. The sample was positioned between the source and near-field detector, which recorded the Debye Scherrer rings of the Cu 111 reflections. From these recordings, a diffraction spot of a single grain was chosen for closer investigation. The near-field detector was removed, giving way to an X-ray objective lens, which consisted of 88 Be parabolic lenses, magnifying the selected grain 17.9 times onto the far-field detector 5.3 m downstream. The far-field detector was a PCO.edge sCMOS camera with 2160 \times 2560 pixels and an indirect X-ray detection scheme. This camera had an internal visible light objective coupled with a scintillator, resulting in a final effective pixel size of 42 nm at the sample.

The images displayed are projections of the chosen Cu grain as the information is integrated along the diffracted beam direction. Two different scanning modes were used in this study: *orientation* and *axial strain scan*. *Orientation scans* measured the crystallographic orientation by rotating around ϕ and χ while keeping a constant $2\theta^{\text{hkl}}$ angle, corresponding to a fixed lattice plane spacing for such a scan. *Axial strain scans* measured 2nd-order strains by rotating around ϕ and $2\theta^{\text{hkl}}$, keeping a constant χ angle. The ϕ axis was tilted in both scanning modes over a minimum range of 2° with a

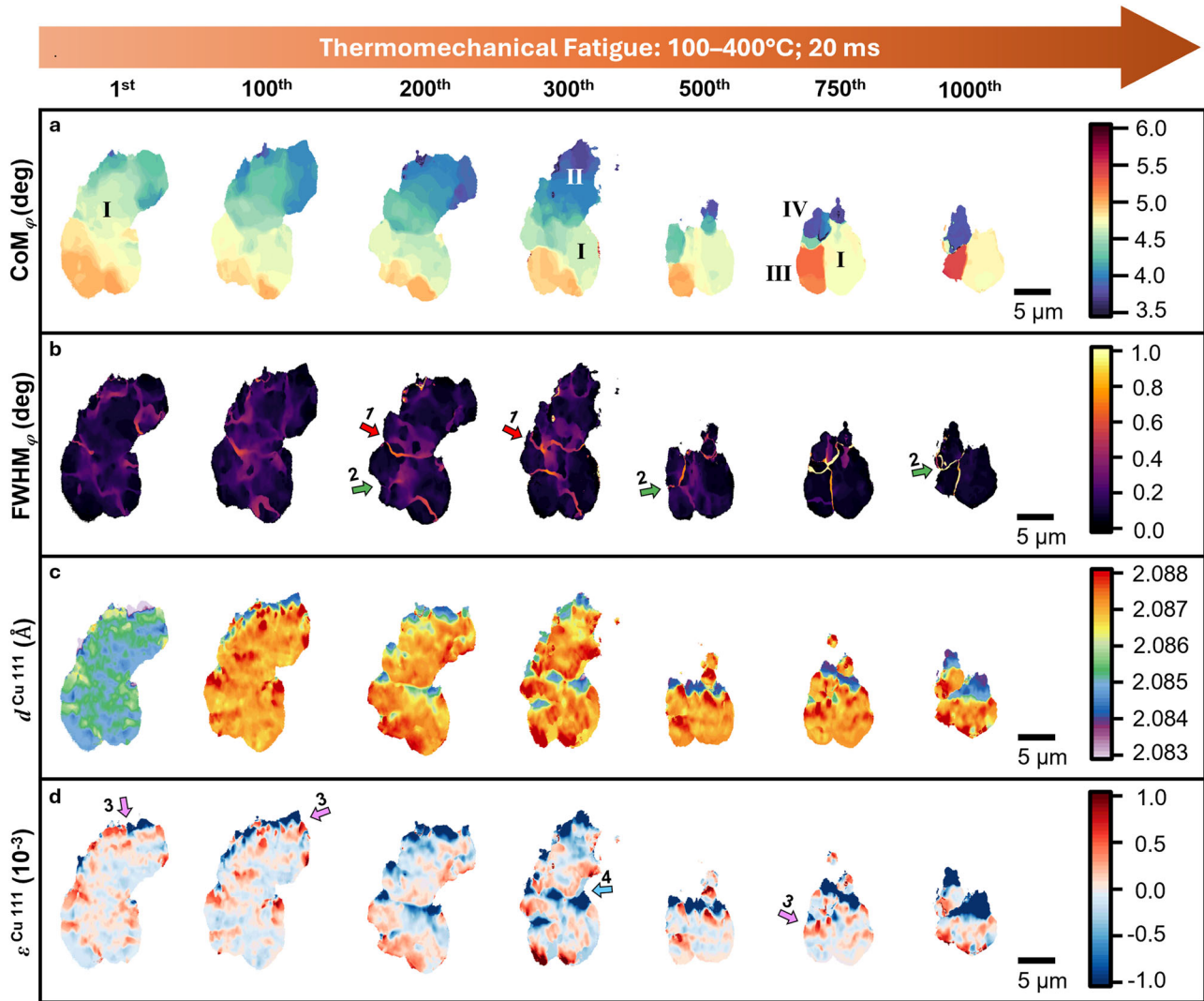


Fig. 10 | Early-stage fatigue during up to thousand 20 ms long heating pulses. Mappings of the axial strain scans at different stages of cycling between 100 and 400 °C, with 20 ms pulse length, are shown. The images display the CoM_φ(a),

FWHM_φ (b), $d^{\text{Cu}111}$ (c), and $\epsilon^{\text{Cu}111}$ (d). The scale bars on the right side of the image are valid for all mappings. The labeled arrows point towards structural features of interest outlined in the main text.

maximum step size of 0.07°. In the *axial strain scans*, the $2\theta^{hkl}$ angle was varied over a range of 0.1° with a step size of 0.005°. The scans were then evaluated using the Python package *darfix*⁴⁶.

The intensity of the Cu 111 reflection at each of the two angles was used to calculate the center of mass (CoM) and full widths at half maximum (FWHM) for each pixel and thereby determine the mean orientation and diffraction angle. From the diffraction angle $2\theta^{hkl}$, the lattice plane spacing of the Cu {111} crystallographic planes was calculated using Bragg’s law:

$$d^{hkl} = \frac{\lambda}{2 \sin(\theta^{hkl})} \quad (3)$$

To calculate the 2nd-order strains (ϵ^{hkl}) the sample an assumption about the stress-free reference state is necessary. For this, the strain-free lattice plane spacing d_0^{hkl} (θ_0^{hkl}) was set equal to the average lattice plane spacing determined for each mapping using a normal distribution function. Hence, we were insensitive to changes in 1st-order strains in Cu, which would have been difficult to calculate anyhow since the relationship between the detector and sample coordinate system was not fully elucidated with the

necessary precision. From this assumption ϵ^{hkl} was calculated accordingly⁴⁷:

$$\epsilon^{hkl} = \frac{d^{hkl} - d_0^{hkl}}{d_0^{hkl}} \approx - \frac{(\theta^{hkl} - \theta_0^{hkl})}{\tan(\theta^{hkl})} \quad (4)$$

20 kHz X-ray diffraction

20 kHz XRD was performed at the ADDAMS beamline of the Swiss Light Source at the Paul Scherrer Institute in Switzerland, using a beam of $1.2 \times 0.1 \text{ mm}^2$ with a photon energy of 14.35 keV⁴⁸. The two-dimensional (2D) X-ray diffraction patterns were collected using an Eiger 1 M detector with a 20 kHz acquisition rate, making the individual exposure time 50 μs. All 2D diffraction patterns were processed using the software package *pyFAI*^{49,50}. The sample was mounted at an upright angle of 55° to the vertical axis of the experimental setup to probe only the central Cu pad and measure the biaxial stress state using a version of the $\sin^2 \psi$ method adapted to the tilt angle (Eq. 5). The derivation of this equation is outlined in¹⁵.

$$\frac{\partial d^{\text{Cu}111}(\delta)}{\partial(\sin \alpha \cos \theta \sin \delta + \cos \alpha \sin \theta)^2} = -\frac{1}{2} S_2^{\text{Cu}111} d_0^{\text{Cu}111} \sigma_{ip} \quad (5)$$

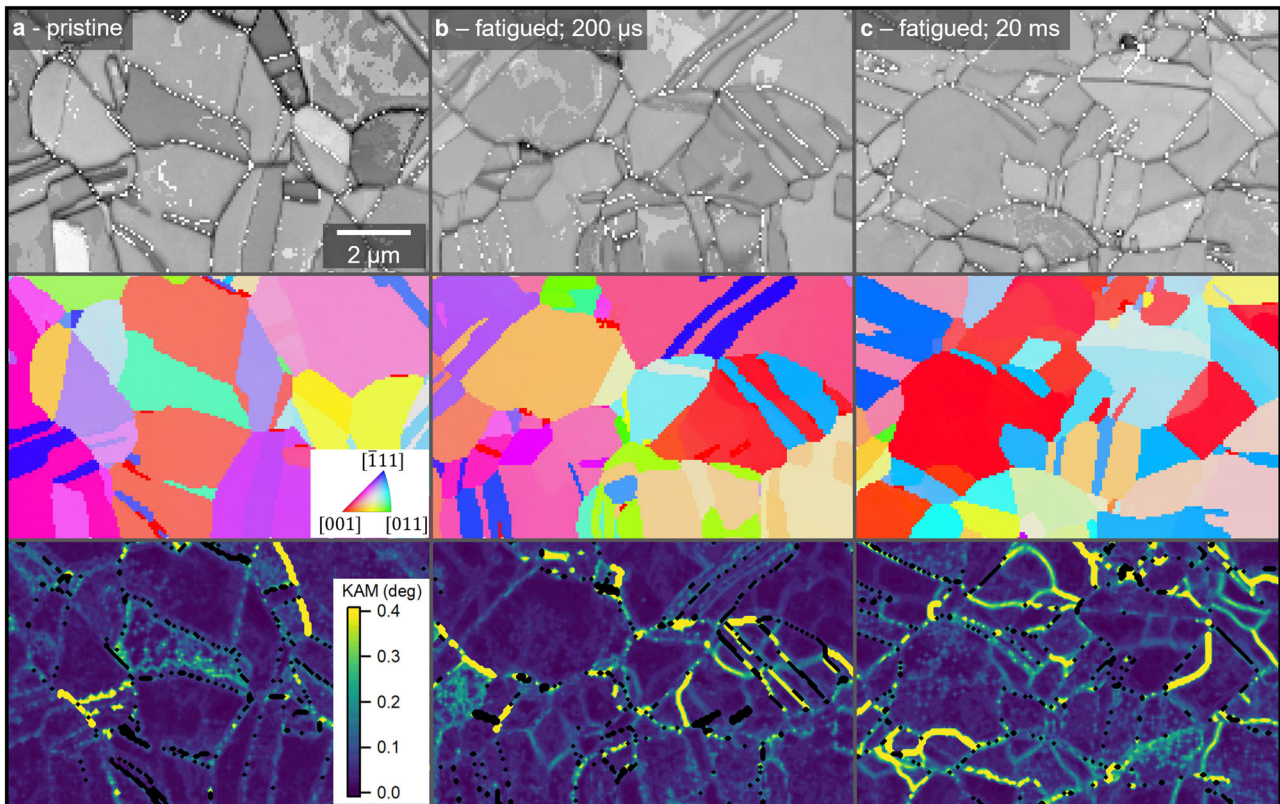


Fig. 11 | HR-EBSD comparison of pristine and cycled Cu thin films. HR-EBSD analysis was performed on a 5 μm thick, pristine Cu thin film (a) and two thin films after 1000 applied cycles between 100 and 400 °C using a pulse length of 200 μs (b)

and 20 ms (c), respectively. From top to bottom, the band channel contrast, orientation, and KAM are shown. The scale bars in (a) are valid for all measurements.

Therein $d^{Cu\ 111}$ is the lattice plane spacing of Cu {111} planes and $d_0^{Cu\ 111}$ is the strain-free lattice plane spacing at thermodynamical equilibrium. The angles α , δ , and θ refer to the tilt angle, azimuthal angle, and Bragg angle, respectively. Finally $-\frac{1}{2}S_2^{Cu\ 111}$ is the X-ray elastic constant for Cu, which was fitted using a Hill grain interaction model and elastic constants taken from literature³¹. Since the data proved to have a considerably low signal-to-noise ratio a moving average smoothing was applied to the stresses calculated, using a window size of 5 values. The strain-free lattice plane spacing $d_0^{Cu\ 111}$ was calculated by finding the azimuthal angle, where:

$$(\sin \alpha \cos \theta \sin \delta + \cos \alpha \sin \theta)^2 = \frac{1}{1 + 2\nu^{Cu\ 111}} = 0.625 \quad (6)$$

Further, the strain-free lattice plane spacing $d_0^{Cu\ 111}$ at different temperatures was used to calculate the temperature of Cu according to its thermal expansion:

$$T = \left[\frac{d_0^{hkl}(T) - d_0^{hkl}(T_{base})}{d_0^{hkl}(T_{base})} \frac{1}{\alpha_{Cu}} \right] + T_{base} \quad (7)$$

The temperature profiles obtained from the incorporated Al sensor and this approach are compared in Supplementary Fig. 4.

Scanning Electron Microscopy

We employed SEM as a complementary tool to characterize the interaction of grains during thermomechanical cycling. Additional *polyheaters* with a Cu film thickness of 5 μm were cycled at similar conditions and electrochemically polished down to a thickness of 2 μm. SEM and HR-EBSD were performed using a Thermo Fisher Apreo 2S with an Oxford c-nano EBSD

detector. The HR-EBSD scan was conducted with a step size of 70 nm in an area of $2 \times 10 \mu\text{m}^2$. The results were evaluated using MTEX (5.10.2), a dedicated MATLAB toolbox, which was used to perform grain reconstruction and characterize grain boundaries using different thresholds of misorientation⁵². The threshold for HAGBs and LAGBs were set to $>15^\circ$ and $<1^\circ$, respectively.

Data availability

Original research data for this work is available upon reasonable request.

Received: 10 April 2025; Accepted: 12 June 2025;

Published online: 01 July 2025

References

1. Nix, W. D. Mechanical properties of thin films. *Metall. Trans. A* **20**, 2217–2245 (1989).
2. Nelhiebel, M. et al. A reliable technology concept for active power cycling to extreme temperatures. *Microelectron. Reliab.* **51**, 1927–1932 (2011).
3. Dibra, D. et al. On the origin of thermal runaway in a trench power MOSFET. *IEEE Trans. Electron Devices* **58**, 3477–3484 (2011).
4. Nelhiebel, M. et al. Effective and reliable heat management for power devices exposed to cyclic short overload pulses. *Microelectron. Reliab.* **53**, 1745–1749 (2013).
5. Kraft, O., Wellner, P., Hommel, M., Schwaiger, R. & Arzt, E. Fatigue behavior of polycrystalline thin copper films. *Z. Für Met.* **93**, 392–400 (2002).
6. Schwaiger, R., Dehm, G. & Kraft, O. Cyclic deformation of polycrystalline Cu films. *Philos. Mag.* **83**, 693–710 (2003).
7. Dehm, G., Balk, T. J., Edonoué, H. & Arzt, E. Small-scale plasticity in thin Cu and Al films. *Microelectron. Eng.* **70**, 412–424 (2003).

8. Zhang, G. P. et al. Length-scale-controlled fatigue mechanisms in thin copper films. *Acta Mater.* **54**, 3127–3139 (2006).
9. Chason, E. et al. Understanding residual stress in electrodeposited Cu thin films. *J. Electrochem. Soc.* **160**, D3285–D3289 (2013).
10. Bigl, S., Wurster, S., Cordill, M. J. & Kiener, D. Advanced characterisation of thermo-mechanical fatigue mechanisms of different copper film systems for wafer metallizations. *Thin Solid Films* **612**, 153–164 (2016).
11. Ghidelli, M., Sebastiani, M., Collet, C. & Guillemet, R. Determination of the elastic moduli and residual stresses of freestanding Au-TiW bilayer thin films by nanoindentation. *Mater. Des.* **106**, 436–445 (2016).
12. Seligmann, B., Alfreider, M., Wurmschuber, M. & Kiener, D. Novel approach for assessing cyclic thermomechanical behavior of multilayered structures. *Adv. Eng. Mater.* **25**, 2201209 (2023).
13. Moser, S. et al. A novel setup for in situ monitoring of thermomechanically cycled thin film metallizations. *JOM* **71**, 3399–3406 (2019).
14. Moser, S. et al. Fatigue of copper films subjected to high-strain rate thermo-mechanical pulsing. *Microelectron. Reliab.* **137**, 114782 (2022).
15. Ziegelwanger, T. et al. 20 kHz X-ray diffraction on Cu thin films explores thermomechanical fatigue at high strain-rates. *Mater. Des.* **251**, 113664 (2025).
16. Hansen, N., Huang, X. & Winther, G. Grain orientation, deformation microstructure and flow stress. *Mater. Sci. Eng. A* **494**, 61–67 (2008).
17. Hughes, D. A. & Hansen, N. The microstructural origin of work hardening stages. *Acta Mater.* **148**, 374–383 (2018).
18. Meng, F., Ferrié, E., Déprés, C. & Fivel, M. 3D discrete dislocation dynamic investigations of persistent slip band formation in FCC metals under cyclical deformation. *Int. J. Fatigue* **149**, 106234 (2021).
19. Lukáš, P. & Kunz, J. L. Role of persistent slip bands in fatigue. *Philos. Mag.* **84**, 317–330 (2004).
20. Zehetbauer, M. J., Steiner, G., Schafner, E., Korznikova, A. V. & Korznikova, E. Deformation induced vacancies with severe plastic deformation: measurements and modelling. *Mater. Sci. Forum* **503–504**, 57–64 (2006).
21. Noell, P., Carroll, J., Hattar, K., Clark, B. & Boyce, B. Do voids nucleate at grain boundaries during ductile rupture? *Acta Mater.* **137**, 103–114 (2017).
22. Noell, P. J., Sills, R. B. & Boyce, B. L. Suppression of void nucleation in high-purity aluminum via dynamic recrystallization. *Metall. Mater. Trans. A* **51**, 154–166 (2020).
23. Noell, P. J., Sabisch, J. E. C., Medlin, D. L. & Boyce, B. L. Nanoscale conditions for ductile void nucleation in copper: Vacancy condensation and the growth-limited microstructural state. *Acta Mater.* **184**, 211–224 (2020).
24. Pineau, A., Benzerga, A. A. & Pardo, T. Failure of metals I: Brittle and ductile fracture. *Acta Mater.* **107**, 424–483 (2016).
25. Wurster, S., Bigl, S., Cordill, M. J. & Kiener, D. Accelerated thermo-mechanical fatigue of copper metallizations studied by pulsed laser heating. *Microelectron. Eng.* **167**, 110–118 (2017).
26. Zhang, P. et al. Low-cycle fatigue-cracking mechanisms in fcc crystalline materials. *Philos. Mag.* **91**, 229–249 (2011).
27. Simons, H. et al. Dark-field X-ray microscopy for multiscale structural characterization. *Nat. Commun.* **6**, 6098 (2015).
28. Jakobsen, A. C. et al. Mapping of individual dislocations with dark-field X-ray microscopy. *J. Appl. Crystallogr.* **52**, 122–132 (2019).
29. Hlushko, K. et al. Dark-field X-ray microscopy reveals mosaicity and strain gradients across sub-surface TiC and TiN particles in steel matrix composites. *Scr. Mater.* **187**, 402–406 (2020).
30. Zelenika, A. et al. 3D microstructural and strain evolution during the early stages of tensile deformation. *Acta Mater.* **270**, 119838 (2024).
31. Zelenika, A. et al. Observing formation and evolution of dislocation cells during plastic deformation. *Sci. Rep.* **15**, 8655 <https://doi.org/10.1038/s41598-025-88262-3> (2025).
32. Hlushko, K. et al. Intragranular thermal fatigue of Cu thin films: Near-grain boundary hardening, strain localization and voiding. *Acta Mater.* **253**, 118961 (2023).
33. Rodríguez-Martínez, J. A., Rodríguez-Millán, M., Rusinek, A. & Arias, A. A dislocation-based constitutive description for modeling the behavior of FCC metals within wide ranges of strain rate and temperature. *Mech. Mater.* **43**, 901–912 (2011).
34. Hahn, T. A. Thermal expansion of copper from 20 to 800 K—Standard Reference Material 736. *J. Appl. Phys.* **41**, 5096–5101 (1970).
35. Watanabe, H., Yamada, N. & Okaji, M. Linear thermal expansion coefficient of silicon from 293 to 1000 K. *Int. J. Thermophys.* **25**, 221–236 (2004).
36. Dean, J., Aldrich-Smith, G. & Clyne, T. W. Use of nanoindentation to measure residual stresses in surface layers. *Acta Mater.* **59**, 2749–2761 (2011).
37. Hoffmann, P. et al. Thermomechanical fatigue damage modeling and material parameter calibration for thin film metallizations. *Int. J. Fatigue* **155**, 106627 (2022).
38. Mishra, A. et al. High-strain-rate response of ultra-fine-grained copper. *Acta Mater.* **56**, 2770–2783 (2008).
39. Jordan, J. L., Siviour, C. R., Sunny, G., Bramlette, C. & Spowart, J. E. Strain rate-dependant mechanical properties of OFHC copper. *J. Mater. Sci.* **48**, 7134–7141 (2013).
40. Wang, Y., Zhang, J., Wei, Q. & Zhao, Y. Grain size effects on the compressibility and yield strength of copper. *J. Phys. Chem. Solids* **74**, 75–79 (2013).
41. Peng, W. et al. Insights into abnormal grain growth in copper thin films for reduced electrical resistivity: A quantitative multi-order-parameter phase-field study under finite element framework. *Acta Mater.* **260**, 119236 (2023).
42. Langer, J. S., Bouchbinder, E. & Lookman, T. Thermodynamic theory of dislocation-mediated plasticity. *Acta Mater.* **58**, 3718–3732 (2010).
43. Lieou, C. K. C. & Bronkhorst, C. A. Thermodynamic theory of crystal plasticity: Formulation and application to polycrystal fcc copper. *J. Mech. Phys. Solids* **138**, 103905 (2020).
44. Ahl, S. R. et al. Ultra-low-angle boundary networks within recrystallizing grains. *Scr. Mater.* **139**, 87–91 (2017).
45. Keckes, J., Hlushko, K., Reisinger, M. & Ziegelwanger, T. *In-Situ Observation of Grain Boundary Formation and Strain Gradient Evolution during Thermal Fatigue of Cu Grains within Cu Interconnects [Data Set]*. European Synchrotron Radiation Facility. <https://doi.org/10.1515/ESRF-ES-899909770> (2021).
46. Garriga Ferrer, J. et al. *darfix* – data analysis for dark-field X-ray microscopy. *J. Synchrotron Radiat.* **30**, 527–537 (2023).
47. Yildirim, C., Jessop, C., Ahlström, J., Detlefs, C. & Zhang, Y. 3D mapping of orientation variation and local residual stress within individual grains of pearlitic steel using synchrotron dark field X-ray microscopy. *Scr. Mater.* **197**, 113783 (2021).
48. Willmott, P. R. et al. The Materials Science beamline upgrade at the Swiss Light Source. *J. Synchrotron Radiat.* **20**, 667–682 (2013).
49. Kieffer, J. & Karkoulis, D. PyFAI, a versatile library for azimuthal regrouping. *J. Phys. Conf. Ser.* **425**, 202012 (2013).
50. Ashiotis, G. et al. The fast azimuthal integration Python library: *pyFAI*. *J. Appl. Crystallogr.* **48**, 510–519 (2015).
51. Brantley, W. A. Calculated elastic constants for stress problems associated with semiconductor devices. *J. Appl. Phys.* **44**, 534–535 (1973).
52. Bachmann, F., Hielscher, R. & Schaeben, H. Texture Analysis with MTEX – Free and Open Source Software Toolbox. *Solid State Phenom.* **160**, 63–68 (2010).

Acknowledgements

We acknowledge the Paul Scherrer Institut, Villigen, Switzerland for providing synchrotron radiation beamtime at beamline ADDAMS-X04SA of the SLS and Nicola Casati for his supervision. Further, we acknowledge access to the synchrotron facilities by the ESRF (European Synchrotron

Radiation Facility) gratefully. This work was funded by the Austrian Research Promotion Agency (FFG, Project No. 905107).

Author contributions

T.Z., M.R. and J.K. designed the project. M. R. prepared the polyheater samples. T.Z., M.R., S.V.P. and J.T. performed the 20 kHz X-ray diffraction and evaluated the data. T.Z. M.R., R.R.L. and C.Y. performed dark-field X-ray microscopy and evaluated the data. M.P. performed the EBSD characterization. M.M., J.T. and J.K. contributed to the data interpretation and revision of the manuscript. T.Z. wrote the manuscript and coordinated contributions by other authors.

Competing interests

The authors declare no competing interests.

Additional information

Supplementary information The online version contains supplementary material available at <https://doi.org/10.1038/s41529-025-00629-z>.

Correspondence and requests for materials should be addressed to T. Ziegelwanger.

Reprints and permissions information is available at <http://www.nature.com/reprints>

Publisher's note Springer Nature remains neutral with regard to jurisdictional claims in published maps and institutional affiliations.

Open Access This article is licensed under a Creative Commons Attribution 4.0 International License, which permits use, sharing, adaptation, distribution and reproduction in any medium or format, as long as you give appropriate credit to the original author(s) and the source, provide a link to the Creative Commons licence, and indicate if changes were made. The images or other third party material in this article are included in the article's Creative Commons licence, unless indicated otherwise in a credit line to the material. If material is not included in the article's Creative Commons licence and your intended use is not permitted by statutory regulation or exceeds the permitted use, you will need to obtain permission directly from the copyright holder. To view a copy of this licence, visit <http://creativecommons.org/licenses/by/4.0/>.

© The Author(s) 2025